A&A 668, A86 (2022)
https://doi.org/10.1051/0004-6361/202244627

Astronomy & Astrophysics

ESPRESSO observations of HE 0107−5240 and other CEMP-no stars with [Fe/H] ≤ −4.5⋆

D. S. Aguado[1,2], P. Molaro[3,4], E. Caffau[5], J. I. González Hernández[6,7], M. R. Zapatero Osorio[8], P. Bonifacio[5], C. Allende Prieto[6,7], R. Rebolo[6,7,9], M. Damasso[10], A. Suárez Mascareño[6,7], S. B. Howell[11], E. Furlan[12], S. Cristiani[3], G. Cupani[3], P. Di Marcantonio[3], V. D'Odorico[3,13,4], C. Lovis[20], C. J. A. P. Martins[15,16], D. Milakovič[3,4,17], M. T. Murphy[18], N. J. Nunes[14], F. Pepe[20], N. C. Santos[21,22], T. M. Schmidt[3,19], and A. Sozzetti[10]

(Affiliations can be found after the references)

Received 29 July 2022 / Accepted 8 October 2022

ABSTRACT

Context. HE 0107−5240 is a hyper metal-poor star with [Fe/H] = −5.39, one of the lowest-metallicity stars known. Its stellar atmosphere is enhanced in carbon, with [C/Fe] = +4.0, without a detectable presence of neutron-capture elements. Therefore, it belongs to the carbon-enhanced metal-poor (CEMP−no) group, along with the majority of the most metal-poor stars known to date. Recent studies have revealed variations in the line-of-sight velocity of HE 0107−5240, suggesting it belongs to a binary system. CEMP-no stars are the closest descendants of the very first Pop III stars, and binarity holds important clues for the poorly known mechanism that leads to their formation.

Aims. We performed high-resolution observations with the ESPRESSO spectrograph at the VLT to constrain the kinematical properties of the binary system HE 0107−5240 and to probe the binarity of the sample of the eight most metal-poor stars with [Fe/H] ≤ −4.5.

Methods. Radial velocities are obtained by using a cross-correlation function in the interval 4200−4315 Å, which contains the relatively strong CH band, against a template that could be either a synthetic spectrum or a combined observed spectrum in an iterative process. A Bayesian method is applied to calculate the orbit using the ESPRESSO measurements and others from the literature. Chemical analysis has also been performed for HE 0107−5240, employing spectral synthesis with the SYNTHE and ATLAS codes.

Results. Observations of HE 0107−5240 spanning more than 3 years show a monotonic decreasing trend in radial velocity at a rate of approximately 0.5 $m\,s^{-1}\,d^{-1}$. A maximum v_{rad} was reached between March 13, 2012, and December 8, 2014. The period is constrained at $P_{orb} = 13\,009^{+1496}_{-1370}$ d. New, more stringent upper limits have been found for several elements: (a) [Sr/Fe] and [Ba/Fe] are lower than −0.76 and +0.2, respectively, confirming the star is a CEMP-no; (b) A(Li) < 0.5 is well below the plateau at A(Li) = 1.1 found in the lower red giant branch stars, suggesting Li was originally depleted; and (c) the isotopic ratio $^{12}C/^{13}C$ is 87 ± 6, showing very low ^{13}C in contrast to what is expected from a 'spinstar' progenitor.

Conclusions. We confirm that HE 0107−5240 is a binary star with a long period of about 13 000 d (∼ 36 yr). The carbon isotopic ratio excludes the possibility that the companion has gone through the asymptotic giant branch phase and transferred mass to the currently observed star. The binarity of HE 0107−5240 implies that some of the first generations of low-mass stars formed in multiple systems and indicates that the low metallicity does not preclude the formation of binaries. Finally, a solid indication of v_{rad} variation has also been found in SMSS 1605−1443.

Key words. stars: abundances – binaries: spectroscopic – stars: Population II – stars: Population III – Galaxy: formation – Galaxy: halo

1. Introduction

HE 0107−5240 is a hyper metal-poor[1] star discovered in the context of the Hamburg/European Southern Observatory (ESO) survey (Christlieb et al. 2001) and first reported by Christlieb et al. (2002a). HE 0107−5240 shows carbon enhancement of [C/Fe] = +4.0 but with no significant n-capture element enrichment. Therefore, it belongs to the class of carbon-enhanced metal-poor stars called CEMP−no, defined as stars with [C/Fe] > 1 and [Ba/Fe] < 0 (Beers & Christlieb 2005). Two years later, Frebel et al. (2005) found a very similar star, HE 1327−2326, with [Fe/H] = −5.6, which prompted a discussion on the frequency of these extremely rare objects (see Cayrel 2005). So far, 14 stars with metallicities [Fe/H] < −4.5 are known. These stars are the objects with the lowest metallicity measured in primitive second generation (Pop II) stars and provide insight into the nature of the first stars and the first chemical production. The iron abundance of these stars is so low that only a few progenitors, possibly even only one, polluted the gas out of which they were formed. The carbon enhancement has been explained as being the result of explosions of faint supernovae (SNe), with energies of 10^{51} erg, together with fallback and mixing (Umeda & Nomoto 2003). An alternative explanation is a double source with lighter elements such as CNO family, synthesised by faint SNe, and heavier elements from more conventional core-collapse SNe (Bonifacio et al. 2015). Spite et al. (2013) noted that the carbon abundance does not follow the iron decrease, but remains rather constant at the lowest metallicity. They suggested the existence of two groups[2]: one with high carbon abundances ([C/H] ≈ −2.0) and a second with lower carbon abundances ([C/H] ≈ −3.5). The former group also shows enhancement of n-capture elements with [Ba/Fe] > 1, which

⋆ Based on ESPRESSO guaranteed time observations collected at the European Southern Observatory under ESO programmes 1102.C-0744, 0103.D-0700, 0104.D-0688, 1104.C-0350, and 108.2268.001 (P.I. P. Molaro).

[1] Following Beers & Christlieb (2005), in this work we use the terms ultra metal-poor, hyper metal-poor, and mega metal-poor to refer to stars with [Fe/H] < −4.0, −5.0, and −6.0, respectively.

[2] Some other authors split CEMP−no stars into two groups depending on [Fe/H] and [C/Fe] (see Yoon et al. 2016, 2019 for more details).

is absent in the latter group. A different origin for carbon has been suggested in the two groups. In the 'high-C' group, both carbon and the n-capture elements come from an asymptotic giant branch (AGB) companion, while the origin of carbon in the 'low-C' band is less certain, but should be pristine and should be coming from the SNe that polluted the gas from which the star was formed. This scenario implies that the high-C group consists of binaries, while the low-C group could be single or binary stars, but without a companion that experienced an AGB phase. This hypothesis has been tested with radial velocity (RV) studies in small samples of metal-poor stars that belong to one of the two groups (Hansen et al. 2016a,b). Additional CEMP stars with [Fe/H] < −4.5 have recently been discovered, revealing that all CEMP stars with [Fe/H] < −4.5 belong to the CEMP-no group (Bonifacio et al. 2018b; Aguado et al. 2018a; Nordlander et al. 2019; González Hernández et al. 2020) and, therefore, are the preferred formation channel for the earliest low-mass star formation.

HE 0107−5240 was employed by several groups to constrain the mass of the very first stars (see e.g. Bonifacio et al. 2003; Schneider et al. 2003; Umeda & Nomoto 2003). The existence of stars such as HE 0107−5240 shows that stars with masses of the order of the Sun or smaller do form at the lowest metallicities. Bromm & Loeb (2003) argued that the significant values of carbon and oxygen could have cooled the gas, thus permitting low-mass star formation. However, the discovery of carbon-normal stars, such as SDSS J1029+1729 (Caffau et al. 2011a), and the discovery of Pristine221.8781+9.7844 (Starkenburg et al. 2018) show that not all extremely metal-poor stars are carbon-enhanced. More complex mechanisms for gas cooling, such as dust cooling or turbulent fragmentation, are required (Schneider et al. 2012; Greif et al. 2012).

The chemical study of HE 0107−5240 is remarkably challenging. Due to the extreme low metallicity, only nine elemental abundances (C, N, O, Na, Mg, Ca, Ti, Fe, and Ni) have been measured so far (Christlieb et al. 2002a, 2004; Collet et al. 2006). Significant upper limits have only been possible for two n-capture elements, [Sr/Fe] < −0.52 and [Ba/Fe] < 0.82 (Christlieb et al. 2004). Understanding the kinematics of HE 0107−5240 is not any simpler: only more than 15 yr after the discovery of HE 0107−5240 was the first indication of binarity found, by Arentsen et al. (2019), which raised the possibility of a mass transfer from an AGB companion. This unexpected binarity behaviour was later confirmed by Bonifacio et al. (2020). Historically, it is interesting to note that the prototype of the CEMP-no star, CS 22957−027, discovered almost simultaneously by Norris et al. (1997) and Bonifacio et al. (1998), has also been shown to be a binary star, with a period of about $P = 3125$ d, by Preston & Sneden (2001).

In this work we continue the RV measurements with the aim to detail the binary properties of this ancient star. At the same time, we monitor the RVs, $v_{\rm rad}$, for other CEMP-no stars with [Fe/H] < −4.5 to assess the fraction of binaries in this group.

2. Espresso observations and data reduction

The Echelle Spectrograph for Rocky Exoplanets and Stable Spectroscopic Observations (Espresso), is a stable fibre-fed échelle spectrograph mounted at the incoherent focus of the Very Large Telescope (VLT) at Paranal Observatory, Chile, designed to measure velocities with precision as high as 10 cm s^{-1} (Pepe et al. 2021). In 2018 we started an ESO guaranteed time observations (GTO) programme (P.I. P. Molaro) to monitor RVs of the most metal-poor stars and probe their binarity. The spectrograph has two fibres with a core diameter of 140 µm, corresponding to a 1.″0 aperture in the sky. While Fibre A was centred on the object, Fibre B was on the sky. The binning of the CCD was initially 2 × 1 pixel and, when it became available, 4 × 2, always with a slow readout mode. Observations were done in single Universal Time (UT) configuration mode with exposure times between $t_{\rm exp} = 1800$ and $t_{\rm exp} = 3600$ s, the maximum allowed by service mode operation. A total of 50 h (time on target) of observation have been carried out during this – still ongoing – programme. The observing conditions were restricted as follows: airmass ≤ 1.5, seeing ≤1.″0, water vapour ≤30 mm, and minimum lunar distance = 30°. Data reduction was performed by the automatic Espresso pipeline, including sky substraction, bias, and flat-fielding correction. The wavelength calibration is the one that combines the ThAr lamp with a Fabry-Pérot etalon (Pepe et al. 2013). The signal-to-noise ratio (S/N) of individual exposures close to the G-band ($\lambda\lambda \sim 4300$ Å) spanned the range $5 \leq S/N \leq 20$, depending on the observing time and the magnitude of the target. We retrieved an additional exposure of HE 0107−5240 taken with the HARPS spectrograph at the ESO 3.6 m telescope. The observation was made in technical time in the high-resolution mode 'HAM'. Observing time was 3600 s and $S/N \sim 2$ at 4300 Å with a seeing of 0.75″.

While our primary target is HE 0107−5240, which has been the subject of 17 visits, the programme also includes Espresso observations for seven more CEMP-no stars with [Fe/H] < −4.5. In Table 1 all the observed targets and their main stellar parameters are summarised. The situation of these primitive stars in the [C/Fe]−[Fe/H] plane is shown in Fig. 1, together with other metal-poor stars that are not included in our programme for various reasons that will be discussed in Sect. 8.

Table 1. Targets observed in our Espresso GTO program.

Star	*Gaia G* (mag)	$T_{\rm eff}$ (K)	log g (cgs)	[Fe/H]	[C/Fe]	RUWE [a]
HE 0107−5240[1]	14.9	5100	2.2	−5.39	4.00	1.01
SDSS J0023+0307[2,3]	17.6	6140	4.8	< − 5.50	>3.31	0.95
HE 0233−0343[4]	15.3	6100	3.4	−4.68	3.32	1.02
SMSS 0313−6708[5]	14.5	5125	2.3	< − 7.10	>5.39	1.02
HE 0557−4840[6]	15.2	4900	2.2	−4.75	1.66	1.07
SDSS J1313−0019[7,8]	15.2	5170	2.6	−5.00	3.00	0.99
HE 1327−2326[9]	13.4	6180	3.7	−5.60	4.26	0.98
SMSS 1605−1443[10]	15.4	4850	2.0	−6.21	3.89	1.06

Notes. [a]The Renormalised Unit Weight Error could be used to detect variability (see text).
References. (1) Christlieb et al. (2002b); (2) Aguado et al. (2018b); (3) Aguado et al. (2019); (4) Hansen et al. (2014); (5) Keller et al. (2014); (6) Norris et al. (2007); (7) Allende Prieto et al. (2015); (8) Frebel et al. (2015); (9) Frebel et al. (2005); (10) Nordlander et al. (2019).

3. Radial velocity determination

The Espresso RV precision allows us to detect binary systems even if they show long periods (up to several decades) and relatively small RV changes in a period of time of a few years.

The measurements of the stellar RVs were performed in two steps. First, a synthetic model with the SYNTHE code (Kurucz 2005; Sbordone 2005) was computed by assuming stellar parameters and abundances from literature values (Christlieb et al. 2004). Then we smoothed and resampled the synthetic spectra to the Espresso (and HARPS) resolving power of $R \sim 140\,000$

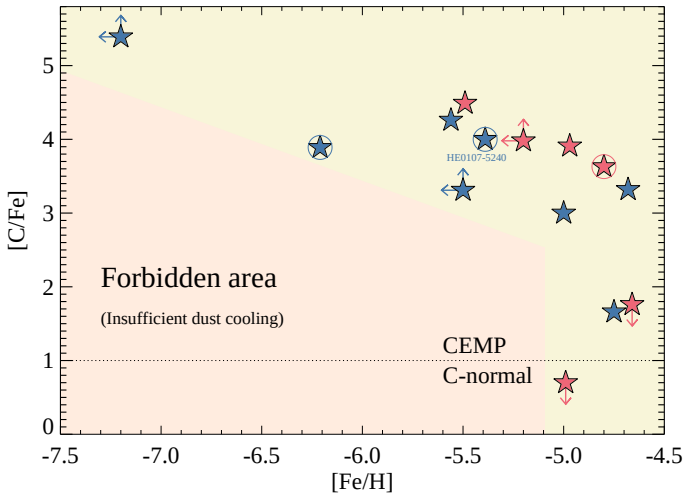

Fig. 1. [C/Fe]−[Fe/H] plane for all the stars observed with ESPRESSO (blue symbols) and for other metal-poor stars (red symbols). Stars with confirmed binarity (HE 0107−5240 and SDSS J0929+0238) and indicated binarity (SMSS 16054−1443) are marked with a circle. The region where no low-mass star formation is permitted, according to Chiaki et al. (2017), is also red-filled.

(and $R \sim 115\,000$) and to the same lambda step. Subsequently, we normalised the observed spectra and interpolated both data and the template to the same wavelength. A cross-correlation function (CCF) was performed in the Fourier space using the algorithm from Tonry & Davis (1979), which contained the `noao.rv` package within the `IRAF`[3] (Tody et al. 1993) environment over the 4200−4315 Å interval, where the CH absorptions are detectable in individual exposures.

Second, we corrected each exposure by the shift derived from the CCF and combined all the spectra in the rest of frame with a 3σ-clip algorithm to compute a high-S/N 'natural' template. An example of this co-added spectrum of HE 0107−5240 is shown in Fig. 2. Similarly to the previous step, we normalised the combined spectrum and calculated a new CCF for each individual exposure, obtaining our final $v_{\rm rad}$ values.

The RVs given by the CCF are summarised in Table 2. Focusing on HE 0107−5240, the average error we have from ESPRESSO data is $13\,{\rm m\,s^{-1}}$, eight times lower than the one from HARPS, $104\,{\rm m\,s^{-1}}$. We also notice that the RV of the #1 ESPRESSO observation taken on September 3, 2018, is in common with Bonifacio et al. (2020), and the two measurements are consistent at the 1.5σ level. This small difference is mostly attributed to the fact that the CCF of Bonifacio et al. (2020) was performed over a different range, 4000−4498 Å, and included other lines that show some velocity offset with respect to the CH molecular absorption. In the next section we present a complete kinematical analysis based on the results we obtained for HE 0107−5240 from ESPRESSO data and from other sources in the literature.

4. Binarity of HE 0107−5240

The RVs of HE 0107−5240 show a monotonically decreasing trend, and therefore we confirm that this is a binary star with a long period. The overall rate of change in this period is $\sim 0.5\,{\rm m\,s^{-1}\,d^{-1}}$, which is consistent with previous results from Arentsen et al. (2019) and Bonifacio et al. (2020).

To constrain the kinematical properties of the binary star HE 0107−5240 together with the ones derived in this work, we took advantage of previous $v_{\rm rad}$ measurements from the UV-Visual Echelle Spectrograph UVES) at VLT (Christlieb et al. 2004), the High-Resolution Spectrograph (HRS) at the Southern African Large Telescope (SALT), and ESPRESSO at VLT (Bonifacio et al. 2020). Verify that your intended meaning has not been changed. The $v_{\rm rad}$ data were binned in 1d bins to limit the stellar jitter. This only affects the UVES data, reducing the number of points from 33 to 17 (see Fig. 3, upper-left panel). The HRS points with $v_{\rm rad}$ errors larger than $2.0\,{\rm km\,s^{-1}}$ have not been included in the upper-middle panel of Fig. 3. All the RVs were modelled using the RADVEL toolkit (Fulton et al. 2018)[4] and including a Keplerian motion of the star plus an RV offset (the γ of the $v_{\rm rad}$ curve) and a jitter parameter for each instrument within a likelihood scheme implemented in python using CELERITE (Foreman-Mackey et al. 2017)[5]. Unfortunately, there are no contemporaneous observations of different instruments, except for the single HARPS RV point, that would allow us to derive any possible RV offset between different instruments, but the jitter may be absorbing part of this possible offset with an uncertainty that propagates onto the uncertainties on orbital period, semi-amplitude velocity, and eccentricity. The Keplerian orbit is described as

$$v_{\rm rad} = \gamma + k_2(\cos(\nu_a + \omega) + e\cos(\omega)), \quad (1)$$

where the true anomaly, ν_a, is related to the solution of the Kepler equation, which depends on the orbital period, P_2, the orbital semi-amplitude velocity, k_2, the argument of periastron, ω, and the eccentricity of the orbit, e. The RADVEL toolkit allows both the time of periastron, $T_{2,\rm peri}$, and the time at inferior conjunction of the star, $T_{2,\rm conj}$, to be inferred. Following Fulton et al. (2018), we chose to perform fitting and posterior sampling using the $\ln P_2$, $T_{2,\rm conj}$, $\sqrt{e}\cos\omega$, $\sqrt{e}\sin\omega$, $\ln k_2$ basis, which helps speed up the convergence. We chose $\ln k_2$ to avoid favouring large k_2 and $\ln P_2$ because P_2 may be long compared with the observational baseline. The $v_{\rm rad}$ errors in Fig. 3 include the jitter of each instrument, and the $v_{\rm rad}$ offset has been subtracted. In addition, we adopted uniform priors for all parameters (see Table 3).

To sample the posterior distributions and obtain the Bayesian evidence of the model (that is, the marginal likelihood, ln Z), we relied on nested sampling using DYNESTY (Speagle 2020)[6]. We initialised a number of live points equal to $N^3(N+1)$ to efficiently sample the parameter space, with $N = 10$ the number of free parameters. The resulting posterior distributions are displayed in Fig. 4 together with the orbital parameters of the star. In the middle panel of Fig. 3 we also show, in grey, a subsample of 300 models randomly selected from the final selection of ∼37 696 Bayesian samples from the posterior distributions displayed in Fig. 4.

The binary mass function can be computed from the masses of the binary component (e.g. Tauris & van den Heuvel 2006)

[3] `IRAF` is distributed by the National Optical Astronomy Observatory, which is operated by the Association of Universities for Research in Astronomy (AURA) under a cooperative agreement with the National Science Foundation.

[4] RADVEL is a Python package for modelling RV time series data, available at `https://radvel.readthedocs.io/en/latest/index.html`

[5] CELERITE is a library for fast and scalable Gaussian process regression in one dimension, available at `https://celerite.readthedocs.io/en/stable/`

[6] DYNESTY is a pure python, MIT-licensed dynamic nested sampling package for estimating Bayesian posteriors and evidence, available at `https://dynesty.readthedocs.io/en/stable/`

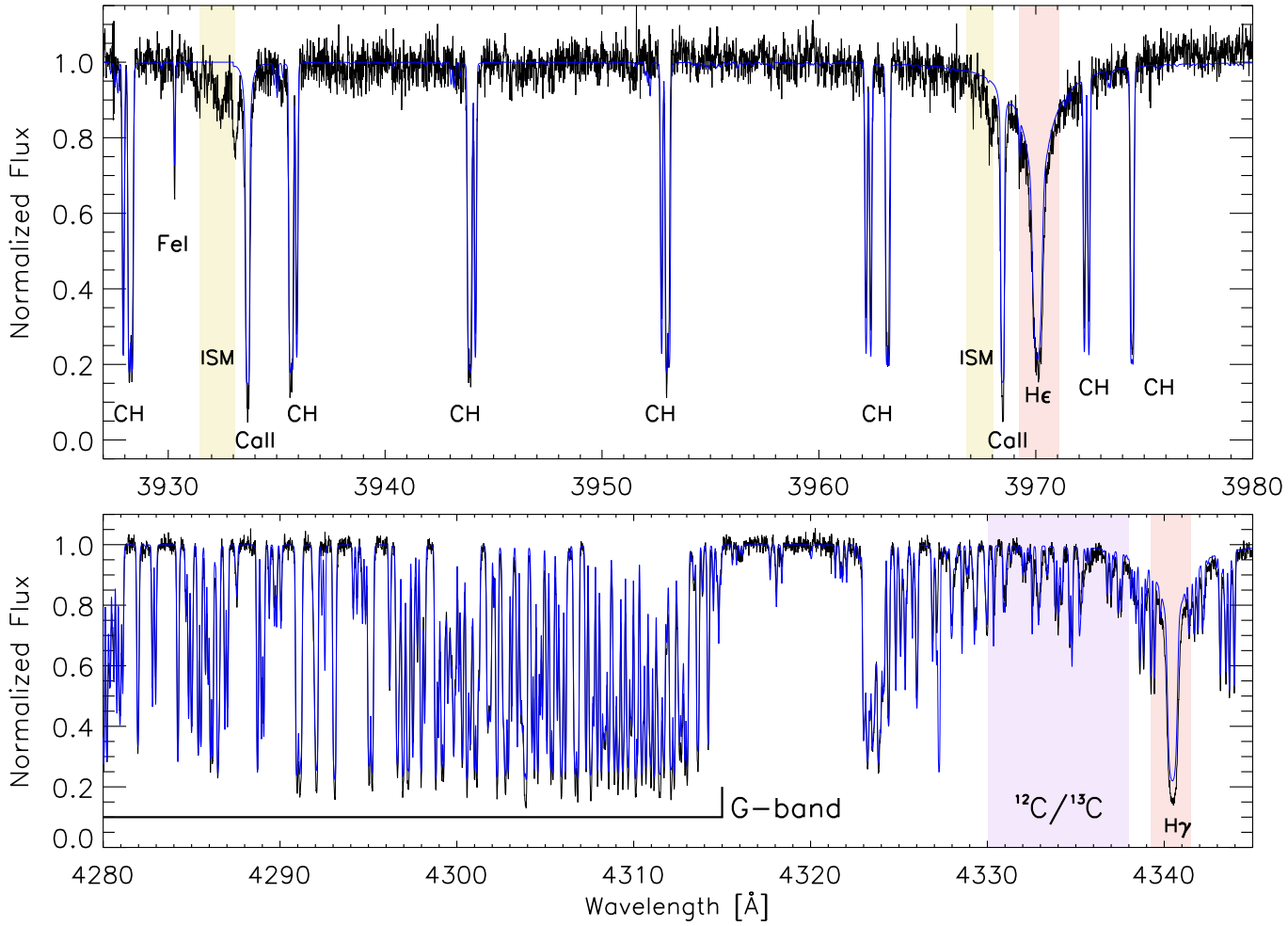

Fig. 2. Narrow region of the co-added ESPRESSO spectrum of HE 0107−5240 (black lines), around the Ca H&K area (*upper panel*), and the *G*-band (*lower panel*) together with a SYNTHE model computed to match the HE 0107−5240 stellar parameters (blue line). Absorptions corresponding to the Balmer series and interstellar Ca II are marked in red and yellow, respectively. Other metallic absorptions and the *G*-band are also labelled.

– that of the seen star, M_2, and that of the unseen binary companion, M_1 – and the orbital parameters as follows:

$$f(M) = (M_1^3 \sin^3 i)/(M_1 + M_2)^2 \quad (2)$$

$$f(M) = [(P_{\rm orb} k_2^3)/(2\pi G)](1 - e^2)^{3/2}. \quad (3)$$

With the Bayesian samples we computed the posterior distribution of the binary mass function, obtaining the following result:

$$f(M) = 0.007^{+0.002}_{-0.001}\,[M_\odot] = 7.0^{+1.7}_{-1.4}\,[M_{\rm Jup}]. \quad (4)$$

Depending on the ratio of masses between the seen and unseen objects of the binary, the binary mass function usually provides a lower limit to the mass of the unseen companion. In general, the minimum mass of this companion can be approximately estimated as the maximum value between f and $f^{1/3} M_2^{2/3}$, thus giving $M_1[M_\odot] > 0.16$ when adopting a mass of $M_2[M_\odot] = 0.8$ for the seen star HE 0107−5240.

The minimum orbital distance (or semi-major axis) of the star with respect to the centre of mass of the binary system can be computed as

$$a_2 \sin i = [(P_{\rm orb} k_2)/(2\pi)](1 - e^2)^{1/2}. \quad (5)$$

The orbital period of the binary is 35.6 ± 4.1 yr. Using the Bayesian samples, we also calculated the posterior distribution of the minimum orbital distance (or semi-major axis of the star's orbit) at $a_2 \sin i = 2.04 \pm 0.30$ AU (see Fig. 4). We note that, as a comparison, Jupiter's orbit in the Solar System shows a semi-major axis of about 5.2 AU and an orbital period of 11.9 yr.

5. Hint of a secondary motion?

The dispersion of the ESPRESSO RVs after subtracting the best fit is 35 m s^{-1}, which is in line with the derived velocity jitter (Table 3). However, this is about three times greater than the mean error bar of the ESPRESSO RV measurements, suggesting the presence of an additional signal with a smaller amplitude. Careful inspection of the ESPRESSO velocity residuals (see the bottom panel of Fig. 3) indicates variability timescales of the order of tens to hundreds of days. We analysed the residuals after the fit using the generalised Lomb-Scargle (GLS) periodogram (Zechmeister & Kürster 2009). The GLS periodogram is an algorithm for detecting periodicities in unevenly sampled time series, the equivalent to a least-squares fitting of sine waves, that generalises the Lomb-Scargle periodogram (Scargle 1982) by including a floating zero point and adding weights to the individual data points. We computed the GLS between 2 and

Table 2. Radial velocities measurements from ESPRESSO.

Star	$v_{\rm rad}$ (km s^{-1})	Error (km s^{-1})	MJD [a] −50 000	Mode	$t_{\rm exp}$ (s)	CCF	Comment [b]
HE 0107−5240	48.049	0.034	8364.107	HR21	3300	CH (*G*-band)	
HE 0107−5240	48.083	0.104	8473.127	–	3600	CH (*G*-band)	HARPS
HE 0107−5240	47.833	0.010	8698.313	HR21	3400	CH (*G*-band)	
HE 0107−5240	47.771	0.010	8721.263	HR21	3400	CH (*G*-band)	
HE 0107−5240	47.786	0.009	8730.206	HR21	3400	CH (*G*-band)	
HE 0107−5240	47.818	0.012	8741.250	HR21	3400	CH (*G*-band)	
HE 0107−5240	47.846	0.012	8759.096	HR21	3400	CH (*G*-band)	
HE 0107−5240	47.697	0.012	9190.096	HR21	3417	CH (*G*-band)	
HE 0107−5240	47.625	0.012	9237.032	HR42	3417	CH (*G*-band)	
HE 0107−5240	47.562	0.018	9427.332	HR21	3600	CH (*G*-band)	
HE 0107−5240	47.533	0.012	9435.176	HR42	3600	CH (*G*-band)	
HE 0107−5240	47.542	0.010	9435.219	HR42	3600	CH (*G*-band)	
HE 0107−5240	47.508	0.013	9489.238	HR21	3000	CH (*G*-band)	
HE 0107−5240	47.505	0.009	9618.061	HR42	3310	CH (*G*-band)	
HE 0107−5240	47.497	0.011	9529.202	HR42	3200	CH (*G*-band)	
HE 0107−5240	47.509	0.008	9545.123	HR42	3200	CH (*G*-band)	
HE 0107−5240	47.436	0.013	9606.042	HR42	3600	CH (*G*-band)	
SDSS J0023+0307	−195.540	0.107	8761.245	HR21	3400	Mg I [b]	Synthetic template
SDSS J0023+0307	−195.035	0.171	8805.034	HR21	3400	Mg I [b]	Synthetic template
SDSS J0023+0307	−195.761	0.102	8835.044	HR21	3400	Mg I [b]	Synthetic template
HE 0233−0343	52.058	0.027	8699.288	HR21	3400	CH (*G*-band)	
HE 0233−0343	52.127	0.021	8760.318	HR21	3400	CH (*G*-band)	
HE 0233−0343	52.169	0.024	8783.112	HR21	3400	CH (*G*-band)	
HE 0233−0343	51.074	0.024	8813.243	HR21	3400	CH (*G*-band)	
SMSS 0313−6708	298.643	0.043	8701.281	HR21	3400	CH (*G*-band)	
SMSS 0313−6708	298.677	0.042	8732.245	HR21	3400	CH (*G*-band)	
SMSS 0313−6708	298.509	0.033	8732.343	HR21	3400	CH (*G*-band)	
SMSS 0313−6708	298.710	0.043	8740.153	HR21	3400	CH (*G*-band)	
SMSS 0313−6708	298.581	0.039	8740.196	HR21	3400	CH (*G*-band)	
SMSS 0313−6708	298.632	0.046	8742.119	HR21	3400	CH (*G*-band)	
SMSS 0313−6708	298.578	0.042	8743.268	HR21	3400	CH (*G*-band)	
SMSS 0313−6708	298.531	0.047	8743.335	HR21	3400	CH (*G*-band)	
SMSS 0313−6708	298.536	0.050	8780.153	HR21	3417	CH (*G*-band)	
SMSS 0313−6708	298.650	0.036	9190.052	HR42	3417	CH (*G*-band)	
SMSS 0313−6708	298.603	0.038	9237.078	HR42	3417	CH (*G*-band)	
SMSS 0313−6708	298.530	0.027	9250.041	HR42	3417	CH (*G*-band)	
SMSS 0313−6708	298.486	0.039	9264.017	HR42	3000	CH (*G*-band)	
HE 0557−4840	212.209	0.028	8761.333	HR21	3400	Mg I [b]	
HE 0557−4840	212.172	0.026	8762.327	HR21	3400	Mg I [b]	
HE 0557−4840	212.199	0.027	8834.084	HR21	3400	Mg I [b]	
HE 0557−4840	212.198	0.023	8864.083	HR21	3400	Mg I [b]	
SDSS J1313−0019	273.984	0.054	9649.249	HR42	3444	CH (*G*-band)	Synthetic template
HE 1327−2326	63.801	0.040	8615.137	HR21	1800	CH (*G*-band)	
HE 1327−2326	63.636	0.037	8688.022	HR21	2700	CH (*G*-band)	
HE 1327−2326	63.709	0.041	8688.055	HR21	2700	CH (*G*-band)	
HE 1327−2326	63.655	0.027	8695.996	HR21	1800	CH (*G*-band)	
HE 1327−2326	63.639	0.037	8697.988	HR21	2400	CH (*G*-band)	
HE 1327−2326	63.697	0.041	8841.331	HR21	1800	CH (*G*-band)	
HE 1327−2326	63.601	0.036	9429.054	HR42	3000	CH (*G*-band)	
HE 1327−2326	63.700	0.016	9663.072	HR42	2844	CH (*G*-band)	
SMSS 1605−1443	−226.059	0.037	9676.277	HR42	3150	CH (*G*-band)	
SMSS 1605−1443	−226.118	0.036	9726.189	HR42	3150	CH (*G*-band)	
SMSS 1605−1443	−226.196	0.037	9727.060	HR42	3150	CH (*G*-band)	
SMSS 1605−1443	−226.214	0.030	9761.059	HR42	3150	CH (*G*-band)	
SMSS 1605−1443	−226.278	0.033	9792.055	HR42	3150	CH (*G*-band)	

Notes. [a]Modified Julian date at the start of observation. [b]Measurements obtained from a synthetic template are indicated (see text for details).

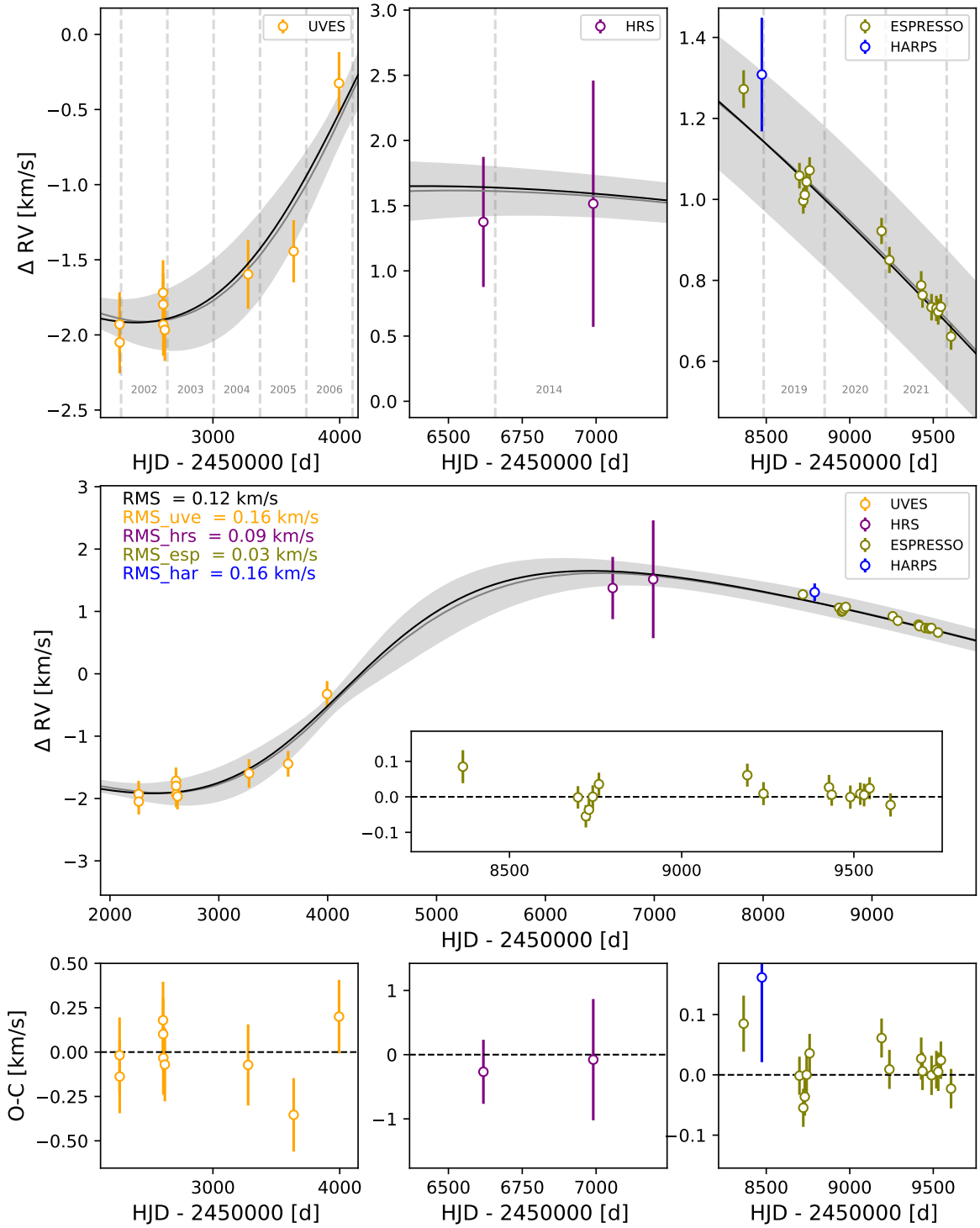

Fig. 3. Radial velocity (RV) points of HE 0107−5240 versus heliocentric Julian date (HJD), together with the best RV model. The inner panel within the *middle panel* shows the ESPRESSO RV points only after removing the best RV model. Within the *middle panel* we provide the RMS of the residuals of all RVs, and those from each spectrograph are given in the *bottom panels*.

1000 d and found no significant peak with a false-alarm probability lower than 10% This is not surprising given the small amount of ESPRESSO data.

One possible scenario to account for the variability in the ESPRESSO velocity residuals is the existence of pulsations in HE 0107−5240. However, oscillations have their characteristic frequency at shorter timescales. Theory predicts that the longest period for first overtone pulsators increases as the metal content decreases, from about 9 d at $Z = 0.0004$ to about 6 d at $Z = 0.004$ (Marconi et al. 2010). Creevey et al. (2019) reported the first detection of Sun-like oscillations in the moderately metal poor giant star HD 122563 (Fe/H] = −2.80 ± 0.15 (Jofré et al. 2014) using hundreds of RV measurements obtained with a mean cadence of one observation per day. They find a characteristic frequency at 3.07 ± 0.05 μHz (3.77 ± 0.06 d) for the oscillations. Interestingly, they also find an additional

signal in the form of a long-term trend with a velocity amplitude and timescale similar to those of HE 0107−5240. In HD 122563, the velocity amplitude and period of the trend are about 120 m s^{-1} and 300 d, respectively. Creevey et al. (2019) favored stellar accretion, activity, and rotation against oscillations to explain the trend because the timescale of the long-term variation is far from the expected intrinsic pulsation periods.

A second scenario is stellar activity that may produce variations in the ESPRESSO RVs modulated by the rotation of the star. Ceillier et al. (2017) find that ≈2% of giant stars are actually fast rotators with rotation periods of less than 170 d. Adopting the mass of 0.8 ± 0.1 $M_\odot$ and the surface gravity of $\log g$[cm s^{-2}] = 2.2 ± 0.1 (Christlieb et al. 2004), the estimated stellar radius of HE 0107−5240 is determined to be $11.8^{+2.2}_{-2.0}$ $R_\odot$, which, combined with periods of 50–200 d (the timescale of the RV variability), would yield equatorial rotational velocities of 2–13 km s^{-1} when the star is seen equator-on. This rotational velocity is measurable with high-resolution spectrographs such as ESPRESSO, but we do not detect any significant rotational broadening in the spectra ($v \sin i \leq 2$ km s^{-1}). This implies that either HE 0107−5240's rotation axis is inclined or periods of ten to a few hundred days are too short for them to be ascribed to the star's rotation. The Transiting Exoplanet Survey Satellite (TESS; Ricker et al. 2015) observed HE 0107−5240 in sectors 2 (August 23 – September 19, 2018) and 29 (August 26 – September 21, 2020). The exposure times were 1426 s for the former and 475 s for the latter. Each TESS sector covers about 25 d (slightly shorter than the timescales of the spectroscopic variability), and the two sectors were observed two years apart. We downloaded the target pixel file products from the Mikulski Archive for Space Telescopes and processed them with Lightkurve software (Barentsen et al. 2021). We find rather flat light curves with no obvious photometric variability higher than ∼5% (confidence of 3 σ). We conclude that with the data in hand, the stellar activity scenario cannot be discarded.

A third scenario is the presence of giant planets around HE 0107−5240 with orbital periods of less than a few hundred days, which are the ones capable of imposing velocity amplitudes of the order of several tens m s^{-1} on their parent star. We explored this hypothesis by fitting one and two Keplerian models with null eccentricity to the ESPRESSO velocity residuals, finding that the two-planet model with velocity amplitudes of ≈30 and 40 m s^{-1} is preferred by the Bayesian statistics. The two planets would have minimum masses of ≈0.5 and 1.0 $M_{\rm jup}$ and orbital periods below 200 d. However, there is neither a sufficient number of RV measurements nor an adequate cadence of the spectroscopic data for a in-depth planetary analysis. Studying this scenario further is beyond the scope of this paper.

We remark, however, that should the presence of giant planets orbiting the hyper metal poor star HE 0107−5240 be confirmed, this would challenge the core accretion theory of planet formation. Heavy elements are needed to cool the gas of the protoplanetary disc and form the dust grains that settle into the midplane and coagulate to create planetesimals (Johnson & Li 2012).

A fourth scenario is actually the mixture of two or more of the above scenarios. More ESPRESSO observations are planned to rule out any of these scenarios or combinations thereof.

6. Improved chemistry of HE 0107−5240

The high quality of the combined spectrum shown in Fig. 2 allows us to perform detailed chemical analysis beyond that in existing works about HE 0107−5240 in the literature. The stellar parameters of this star, $T_{\rm eff}$ = 5200 K, $\log g$ = 2.2, and the microturbulence, $v_{\rm mic}$ = 2.2 km s^{-1}, are taken from Christlieb et al. (2004). We computed different stellar models using the SYNTHE code (Kurucz 2005; Sbordone 2005) along with the ATLAS9 model atmosphere code. We measured 21 Fe I lines from ESPRESSO data (see Table 4), leading to a A(Fe I) = 1.96 ± 0.13. By assuming A(Fe I)$_\odot$ = 7.52 (Caffau et al. 2011b; Lodders 2019), we end up with [Fe/H] = −5.56 ± 0.13, while the preferred metallicity originally reported by Christlieb et al. (2004) was [Fe/H]$_{\rm LTE}$ = −5.39 ± 0.20. In Table 4 the lines and the derived abundances are reported and compared with those of Christlieb et al. (2004). The general abundances are confirmed, and some more lines are observed. In general, the derived abundances are slightly lower than those originally derived. Few significant improvements are obtained. The measured ^{12}C/^{13}C ratio implies that the star is unmixed (i.e. chemically unmixed; Spite et al. 2006, their Fig. 3c). The previous upper limits of [Sr/Fe] ≤ −0.52 and [Ba/Fe] ≤ +0.82 (Christlieb et al. 2004) are now improved to [Sr/Fe] ≤ −0.76 and [Ba/Fe] ≤ +0.20. In particular, these improved values now allow HE 0107−5240 to be classified as a CEMP-no star with confidence, which requires [Ba/Fe] < 1.0. The upper limit on the lithium is now determined to be A(Li)< 0.5. In Fig. 5 we show our new ^{12}C/^{13}C measurement and the more constraining upper limits on Li, Sr, and Ba.

Table 3. Orbit parameters of HE 0107−5240 from the Markov chain Monte Carlo (McMC) analysis.

Parameter	McMC priors	Results
	Keplerian orbit	
k_2 [km s^{-1}]	$\mathcal{LU}$ (0.1, 5)	$1.78^{+0.16}_{-0.11}$
P_2 [d]	$\mathcal{LU}$ (1000, 75 000)	$13\,009^{+1496}_{-1370}$
$T_2 - 2\,450\,000$ [d]	$\mathcal{U}$ (−4000, 3500)	-1630^{+1246}_{-1438}
ω [rad]	$\mathcal{U}$ ($-\pi$, π)	$-1.81^{+0.27}_{-0.41}$
e	$\mathcal{U}$ (0, 1)	$0.31^{+0.11}_{-0.10}$
	Other terms	
Jitter$_{\rm UVES}$ [km s^{-1}]	$\mathcal{LU}$ (0.01, 5.0)	$0.21^{+0.06}_{-0.05}$
Jitter$_{\rm HRS}$ [km s^{-1}]	$\mathcal{LU}$ (0.01, 5.0)	$0.09^{+0.29}_{-0.07}$
Jitter$_{\rm ESPRESSO}$ [km s^{-1}]	$\mathcal{LU}$ (0.01, 5.0)	$0.03^{+0.01}_{-0.01}$
Jitter$_{\rm HARPS}$ [km s^{-1}]	$\mathcal{LU}$ (0.01, 5.0)	$0.09^{+0.24}_{-0.07}$
$\gamma - 46.5$ [km s^{-1}]	$\mathcal{U}$ (−3.0, 3.0)	$0.27^{+0.14}_{-0.19}$

7. Speckle observations of HE 0107−5240

HE 0107−5240 is a binary system, but the mass and nature of the companion are uncertain. A giant is excluded since it would outshine any unevolved companion (Bonifacio et al. 2020). Arentsen et al. (2019) suggested that the companion is a white dwarf that, in its AGB phase, transferred mass to the currently observed giant. Unfortunately, the spectral energy distribution of HE 0107−5240 does not provide useful indications for the companion star. HE 0107−5240 is detected in the *NUV* filter ($\lambda_{\rm eff}$ = 213.6 nm) but not in the *FUV* filter ($\lambda_{\rm eff}$ = 153.9 nm) of the GALEX survey (Bianchi et al. 2011). Venn et al. (2014) explored the spectral energy distribution from 444 nm to 22 080 nm, claiming a marginal detection of an IR excess in the WISE *W*3 band ($\lambda_{\rm eff}$ = 11 560 nm).

In order to set further limits on the nature of the companion star, we exploited speckle imaging on the Gemini 8 m telescope, which provides an angular resolution equal to the

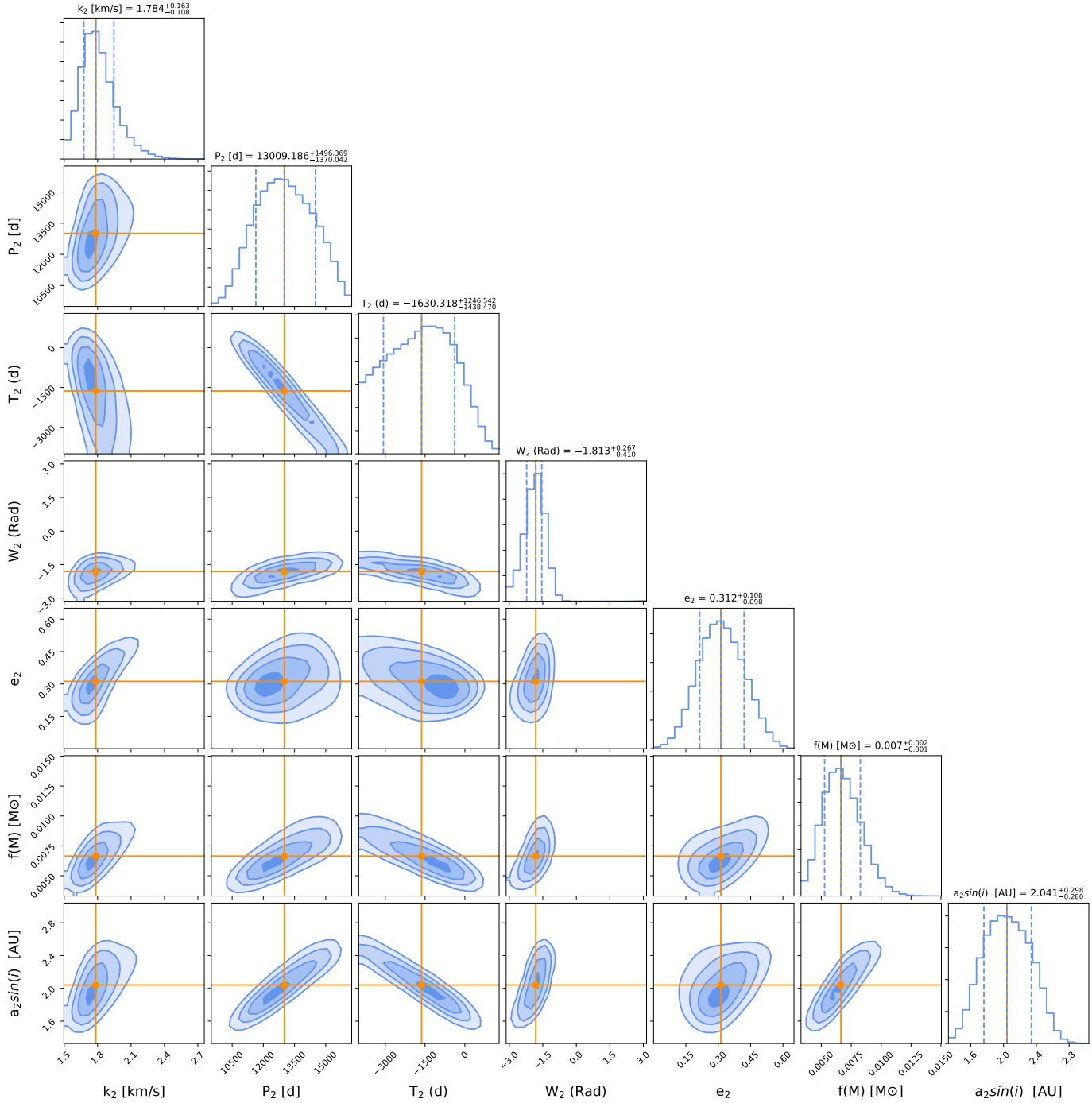

Fig. 4. Posterior distributions of the star's orbital parameters of the RV model and two additional parameters: the binary mass function, $f(\mathrm{M})$, and the star's orbital distance to the centre of mass, $a_2 \sin i$, inferred from the orbital parameters.

diffraction limit of the telescope and fairly deep image contrast levels. We observed HE 0107−5240 on September 16, 2019 UT and October 8, 2019 UT using the Zorro speckle instrument mounted on the 8 m Gemini-South telescope located on Cerro Pachon, Chile (Scott et al. 2021; Howell & Furlan 2022). Zorro uses a dichroic to split the optical light at 674 nm and obtains simultaneous blue and red images on two Andor EMCCD detectors. Both observations of HE 0107−5240 gave consistent results, but the October observations occurred under better seeing, and thus the image contrast achieved was slightly greater. The October 8, 2021 UT observation consisted of a total on-source time of 15 min bracketed by observations of point-spread-function standard stars HR 0242 and HR 0667. The observation collected 1200 images of 60 ms, which were then subjected to Fourier analysis techniques and used to search for close companions to determine their properties and provide reconstructed high-resolution images (see Howell et al. 2011).

Figure 6 shows the achieved image contrast curves (differential magnitude as a function of the projected angular separation to the central star) for the October 2019 HE 0107−5240 observation. The angular limits extend from the 8 m diffraction limit, near 20 mas, out to the speckle correlation limit near 1.2 arcsec. No companion star was detected with differential magnitudes of less than 4 mag (562 nm) and 5.8 mag (832 nm)

Table 4. Abundances of HE 0107−5243 from the ESPRESSO spectrum.

Specie	ion	λ(Å)	A(X)$_\odot$ [1]	A(X)	A(X)$_{Ch04}$	R.I.	[X/Fe] [2]	Notes
Li	3.00	6707.76	1.04	<0.50	<1.1	–	–	
C	6.00	*G*-band	8.58	6.90	6.81	–	+3.88	
^{12}C/^{13}C	6.00	*G*-band	91.4	87	~60	–	–	
N	7.00	CN	8.00	5.00	5.22	–	+2.56	
Na	11.00	5889.951	6.28	1.62	1.83	–	+0.90	
Na	11.00	5895.924		1.62	1.90	–	+0.90	
Mg	12.00	3829.355	7.50	2.15	–	0.47	+0.21	
	12.00	3832.304		2.22	–	0.34	+0.29	
	12.00	3838.292		2.09	–	0.23	+0.15	
	12.00	5167.321		2.33	–	0.88	+0.39	
	12.00	5172.684		2.31	2.38	0.65	+0.37	
	12.00	5183.604		2.31	2.45	0.53	+0.37	
Al	13.00	3961.520	6.41	<0.90	<0.93	0.58	<+0.05	
K	19.00	7698.964	5.10	<1.22	–	–	<+1.68	
Ca	20.01	3933.663	6.34	1.39	1.44	0.15	+0.61	
	20.01	3968.469		1.47	–	0.15	+0.69	
	20.00	4226.728		0.78	0.99	0.63	+0.00	*G*-band
Cr	24.00	5204.511	5.62	<1.07	–	0.99	<+1.01	
	24.00	5206.023		<0.87	–	–	<+0.81	
	24.00	5208.425		<0.67	–	0.97	<+0.61	
Fe	26.00	3820.425	7.52	1.71	1.91	0.23	–0.25	
	26.00	3824.444		2.01	2.30	0.49	+0.05	
	26.00	3825.881		1.73	1.99	0.32	–0.23	
	26.00	3827.822		1.93	–	0.70	–0.03	
	26.00	3834.222		1.85	–	0.51	–0.11	H wing
	26.00	3859.911		1.79	2.08	0.19	–0.17	
	26.00	3878.573		2.04	–	0.57	+0.08	CN
	26.00	3886.282		1.98	–	0.36	+0.20	CH
	26.00	3899.707		2.13	–	0.66	+0.19	
	26.00	3922.912		2.18	2.24	0.71	+0.22	
	26.00	3930.297		2.11	–	0.70	+0.15	
	26.00	4045.812		1.90	2.03	0.52	–0.06	
	26.00	4063.594		1.92	2.00	0.69	–0.04	
	26.00	4071.738		1.97	2.17	0.76	+0.01	
	26.00	4143.868		1.95	–	0.89	–0.01	
	26.00	4202.029		2.14	–	0.92	+0.18	
	26.00	4250.787		1.88	–	0.94	–0.08	*G*-band
	26.00	4325.762		1.91	–	0.76	–0.05	*G*-band
	26.00	4383.545		1.93	–	0.58	–0.04	*G*-band
	26.00	5269.537		2.08	2.20	0.91	+0.12	
	26.00	5328.039		2.08	–	0.94	+0.12	
Sr	38.01	4077.709	2.92	<−3.40	<−2.83	0.48	<–0.76	
	38.01	4215.519		<−3.40	<−2.53	0.65	<–0.76	
Ba	56.01	4554.029	2.19	<−3.17	–	0.91	<+0.20	
	56.01	4934.076		<−2.87	<−2.33	0.95	<+0.50	

Notes. In the 6th column the abundances from Christlieb et al. (2004) are given for comparison. In the column for comments some possible blends are indicated. [1]Solar abundances from Lodders (2019). [2]Chemical ratios, [X/Fe], are based in our derived LTE metallicity: [Fe/H] = −5.56 ± 0.13.

around HE 0107−5240. Any fainter source would have not been seen by the Speckle observations. This is not surprising given the distance to HE 0107−5240 of ≈11 Kpc, as the angular limits of 20 mas to 1.2 arcsec correspond to a linear distance of about 220 AU to 13,200 AU from the primary. The inner working angle distance is not far from the approximate distance of a secondary clump (≈150 AU) in the Becerra et al. (2015) simulations of protostar formation from clouds with primordial chemistry but is much higher than the few AU of the kinematical motion described in Sect. 4.

8. Follow-up of CEMP-no stars with [Fe/H] < −4.5

At the time of writing, there were 12 CEMP-no stars and 2 carbon-normal stars with [Fe/H] < −4.5. As part of the same GTO ESPRESSO programme, in addition to HE 0107−5240, we targeted seven other relatively bright CEMP-no stars located in the most metal-poor regime. The remaining six objects already identified as primitive stars with [Fe/H] < −4.5 have not been observed in this programme for various reasons. For the sake of completeness, we briefly comment on them.

SDSS J1035+0641 (G_{mag} = 18.4, [Fe/H] < −5.3) and SDSS J1742+2531 (G_{mag} = 18.6, [Fe/H] = −4.8) were discovered by Bonifacio et al. (2015, 2018b) and are CEMP stars too faint to be observed with ESPRESSO in a reasonable amount of time. SDSS J1029+1729 (G_{mag} = 16.5, [Fe/H] = −4.73, Caffau et al. 2011a) and Pristine_221.8781+9.7844 (G_{mag} = 16.2, [Fe/H] = −4.66, Starkenburg et al. 2018) show no CH absorptions, and only an upper limit for carbon abundance has been provided. This carbon-normal population was beyond the scope of this project. SDSS J0929+0238 (G_{mag} = 17.9, [Fe/H] = −4.97; Bonifacio et al. 2015) has been proved to be not a binary but a multiple CEMP system (Caffau et al. 2016). Finally, SDSS J0815+4729 (G_{mag} = 16.7, [Fe/H] = −5.5, Aguado et al. 2018a; González Hernández et al. 2020) is an extremely carbon-enhanced star but is not visible from Paranal.

We also note that for our eight stars observed with ESPRESSO, the re-normalised unit weight error (RUWE) published by *Gaia* Early Data Release 3 (Gaia Collaboration 2021) is around 1 in all cases (see Table 3) and far below 1.4 in any case. Therefore, no binarity could be detected by means of RUWE data. In the following we show the results from our follow-up ESPRESSO observations of the other seven CEMP-no stars with [Fe/H] < −4.5.

8.1. SDSS J0023+0307

First reported by Aguado et al. (2018b) and subsequently observed at high resolution (Aguado et al. 2019; Frebel et al. 2019), J0023−0307 is a [Fe/H] < −6.1 dwarf star with no iron lines detected yet. We visited J0023−0307 three times during the period October to December 2019 with an approximately one month interval between observations, which were carried out with the same setup. This star is faint (G_{mag} = 17.6), and therefore only the prominent Mg I b lines were marginally detected. Consequently, the CCF can only be computed with a synthetic template, and the errors are large (~150 m s^{-1}). All three v_{rad} measurements obtained with ESPRESSO are consistent with literature values (−195.5 ± 1.0 and −194.6 ± 1.2 km s^{-1} for Aguado et al. 2019 and Frebel et al. 2019, respectively). Therefore, no evidence for RV variation is shown by the measurements. We report the ESPRESSO values in Table 2, but this object is not included in Fig. 7 for the sake of clarity.

8.2. HE 0233−0343

This turn-off star with [Fe/H] = −4.68 (Hansen et al. 2014) and G_{mag} = 15.3 was observed four times between August and October 2019. The *G*-band around 4330Å is detected in the ESPRESSO spectra and was used for a cross-correlation with the natural template. As a result, the four observations, with an average value of 52.107 km s^{-1}, are compatible at the 2σ level. Hansen et al. (2014) reported v_{rad} = 64 km s^{-1} from high-resolution UVES data. To confirm this hint of variability, we retrieved the UVES data from ESO archive programme ID 69.D-0130(A). Following a similar approach as with the ESPRESSO data, we derived v_{rad} = 52.0 ± 0.6, 51.7 ± 0.6, and 51.4 ± 0.6 km s^{-1} from three existing UVES spectra. This completely agrees with the ESPRESSO measurements summarised in Table 2. We speculate that the measurement from Hansen et al. (2014) does not account for the barycentric correction, which is between V_{bar} = −10.5 and -12.0 km s^{-1}, that would explain the

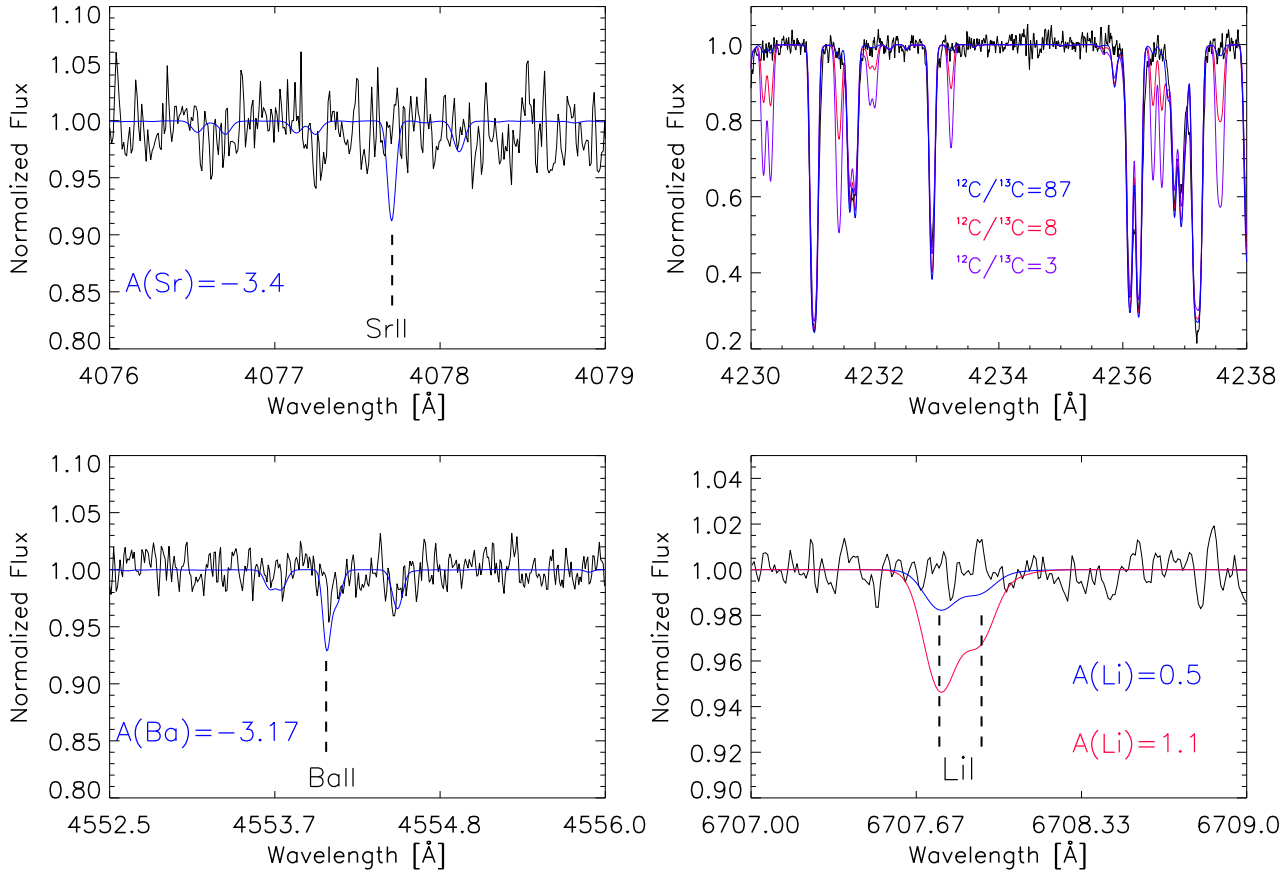

Fig. 5. Narrow region of the ESPRESSO combined spectrum of HE 0107−5240 around the Sr II line at 4077.7 Å (*upper left*), the *G*-band (*upper right*), the Sr II line at 4554.0 Å (*lower left*), and the Li doublet at 6707.8 Å (*lower right*). Derived values and adopted upper limits are shown in blue. Remarkably, at the ESPRESSO resolution the asymmetry in the profile of the Li doublet is clear and the upper limit (A(Li) < 0.5) is much more constraining than the UVES value from Christlieb et al. (2004) (A(Li) < 1.1) in red.

discrepancy. Further observations would be required to verify longer-term binarity.

8.3. SMSS 0313−6708

At the time of writing, SMSS 0313−6708 was the most iron-poor star known, with [Fe/H] < −7.3 and $G_{\rm mag}$ = 14.5. This target was visited ten times in the period August 2019–February 2021. Three observations were repeated on the same nights but removed from the $v_{\rm rad}$ series since they are of significantly lower quality than the other observations. The first group of data, corresponding to 2019, seems consistent, with no variation, while the measurements in 2012 provide slight hints of decreasing behaviour (see Fig. 7). All together, the measurements are consistent, with no variation at the 2σ level, but further observations could provide a more complete picture regarding whether this star is a large-period binary system. The chemistry associated with these observations will be published in a separate article.

8.4. HE 0557−4840

Identified by Norris et al. (2007), this evolved ultra metal-poor star with [Fe/H] = −4.75 and $G_{\rm mag}$ = 15.2 was observed with ESPRESSO on three different nights in the period October 2019–January 2020. Due to the weakness of CH absorptions in the *G*-band, the CCF was built around the Mg I b region, and the $v_{\rm rad}$ measurements are fully compatible with an average of 212.2 km s^{-1} (see Fig. 7). Other measurements from the bibliography included in Norris et al. (2007) and Arentsen et al. (2019) report a similar mean value, though with larger error bars at the level of 1 km s^{-1}

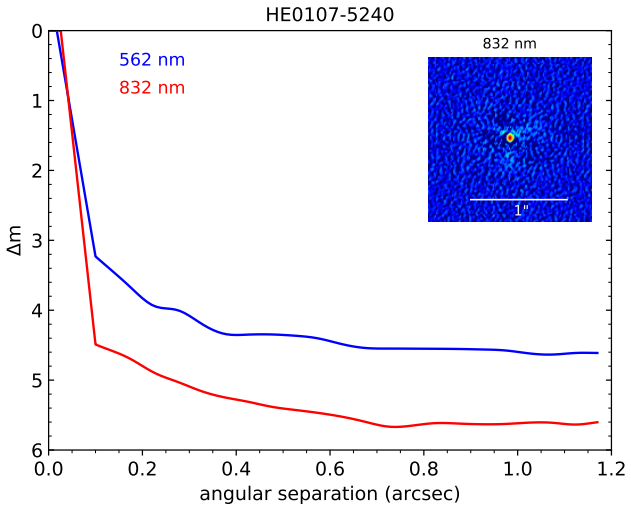

Fig. 6. Our final 5σ contrast curves, in 562 nm and 832 nm, i.e. the limiting magnitude reached in each filter as a function of angular distance from the diffraction limit out to 1.2 arcsec. The inset shows the 832 nm speckle interferometric reconstructed image, in which the brighter primary component is at the centre.

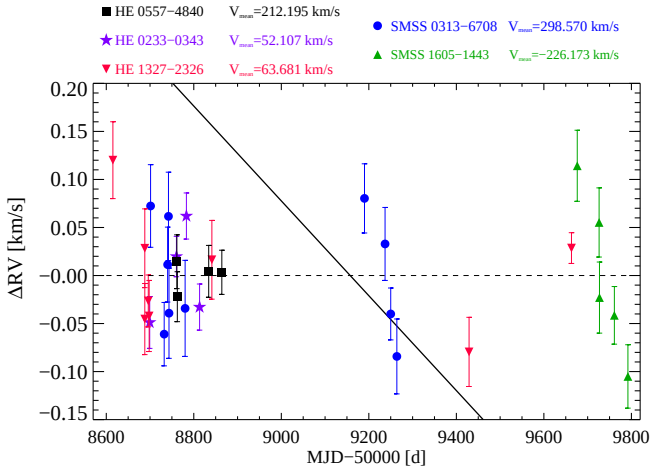

Fig. 7. Summary of the v_{rad} ESPRESSO measurements discussed in Sect. 8, in which the baseline is the average for each star for display purposes. The stars are shown with different colours and symbols: the black squares are for HE 0557−4840 with a mean velocity taken at 212.195 km s^{-1}; the violet stars are for HE 0233−0343 with $(v_{rad})_{mean}$ = 52.107 km s^{-1}; red downward triangles are for HE 1327−2326 with $(v_{rad})_{mean}$ = 63.681 km s^{-1}; the blue dots are for SMSS 0313−6708 with $(v_{rad})_{mean}$ = 298.560 km s^{-1}; and the green upward triangles are for SMSS 1605−1443 $(v_{rad})_{mean}$ = −226.173 km s^{-1}. Errors are 1σ. For reference, the black line crossing the panel is the average variation of HE 0107−5240 in the same interval.

8.5. SDSS J1313−0019

SDSS J1313−0019, G_{mag} = 16.4, was discovered by Allende Prieto et al. (2015) and later studied by Frebel et al. (2015) and Aguado et al. (2017). According to the high-resolution data from Mike at Magellan (Frebel et al. 2015), this evolved star is [Fe/H] = −5.00, is highly carbon-enhanced, [C/Fe] = +3.0, and shows v_{rad} = 274.6 km s^{-1} (no error bars were reported). We observed it just once in March 2022 – 6 yr after the initially discovery – and find v_{rad} = 273.98 ± 0.05 km s^{-1}. The observed difference (∼620 m s^{-1}) is clearly smaller than the most optimistic uncertainty from the Mike observations (1 − 2 km s^{-1}). Furthermore, by cross-matching this object with the Survey of Surveys database (Tsantaki et al. 2022), we find v_{rad} = 273.054 ± 4.498 km s^{-1} from Sloan Extension for Galactic Understanding and Exploration (SEGUE) data, in perfect agreement with those from high-resolution observations. There are, however, other measurements from low-resolution observations reported by Allende Prieto et al. (2015), v_{rad} = 268 ± 6 km s^{-1} (July 2008, SEGUE) and v_{rad} = 242 ± 4 km s^{-1} (March 2014, BOSS). While both SEGUE values are consistent with the Mike and ESPRESSO data, the Baryon Oscillation Spectroscopic Survey (BOSS) measurement (which is closer in time) seems to be incompatible. That fact led Allende Prieto et al. (2015) and Frebel et al. (2015) to suggest that SDSS J1313−0019 could be a binary system. However, the large uncertainty given by the low-resolution data and the fact that the two high-resolution measurements are largely compatible do not allow us to claim v_{rad} variability. Alternatively, the data in hand do not completely preclude some binarity behaviour; more ESPRESSO measurements are required.

8.6. HE 1327−2326

Firstly studied by Frebel et al. (2005), this hyper metal-poor star, with [Fe/H] = −5.60 and G_{mag} = 13.4, was observed nine times between May 2019 and March 2022. Despite the observations spanning three years, no evidence of variability is found. The second observation (see Fig. 7) deviates from the main value by more than 2σ, but the quality of this spectrum was much lower than the others due to poor observing conditions. As in the case of SMSS 0313−6708, the chemical analysis of the combined spectrum will be published separately in a forthcoming paper.

8.7. SMSS 1605−1443

SMSS 16054−1443 is a recent mega metal-poor halo giant discovered by Nordlander et al. (2019) with the SkyMapper telescope. With G_{mag} = 15.4 and a metallicity of [Fe/H] = −6.2 (1D local thermal equilibrium), it has the lowest abundance of iron ever detected in a star. The star is strongly carbon-enhanced, [C/Fe] = 3.9, and has no significant s− or *r*-process enrichment, [Sr/Fe] < 0.2 and [Ba/Fe] < 1.0; as such, it is very likely a CEMP-no star. Nordlander et al. (2019) reported v_{rad} = −224 km s^{-1} from observations with the Mike at Magellan telescope in September 2018, although no error bars were provided. Based on our experience, a reasonable uncertainty for that measurement could be of the order of 1−2 km s^{-1}. Forty-three months later, we detected a difference of ∼2 km s^{-1} from five ESPRESSO measurements, $(v_{rad})_{mean}$ = -226.173 km s^{-1} (see Table 2). Therefore, we can expect a decrease rate of ∼1.6 m s^{-1} d^{-1}. Our observations span ∼115 d and show a decrease of ∼219 m s^{-1} (see Fig. 7), giving a rate of approximately ∼1.9 m s^{-1} d^{-1}, which is about consistent with the rate derived comparing Mike and ESPRESSO data. We find this result convincing and tentatively propose that SMSS 16054−1443 could be another system similar to HE 0107−5240 but varying three times faster. More ESPRESSO observations are required to confirm this hypothesis and calculate orbital parameters.

9. Discussion

9.1. Binarity of our CEMP-no sample

We have probed eight of the most extreme metal-poor CEMP-no stars for binarity by means of very accurate RV measurements obtained with ESPRESSO, and we only find clear evidence for binarity in the case of HE 0107−5240. For this star, Suda et al. (2004) invoked mass transfer from a companion AGB in a similar manner as to what is believed to happen in CEMP-*s* stars (i.e. stars with [Ba/Fe] > 1). Moreover, Arentsen et al. (2019) suggested the presence of a RV variation from a comparison of the UVES observations with some observations taken at the HRS on the SALT Telescope. They noted that the RV of HE 0107−5240 was almost 4 km s^{-1} larger than at the discovery time. On the basis of possible binarity, Arentsen et al. (2019) suggested that the enhancement in carbon could have been the result of mass transfer from the companion star. The period derived here for HE 0107−5240 is so long and the minimum mass of the companion so low that any interaction or mass exchange between the two stars of the system is very unlikely. The result for HE 0107−5240 and for the seven other stars is therefore consistent with the CEMP-no stars being either single or in binary systems with low-mass companions, as found by Hansen et al. (2016a,b) from a sample of more metal-rich CEMP-no stars.

9.2. Stellar structure of HE 0107−5240

HE 0107−5240 lies at the position of the lower red giant branch (LRGB) in the $T_{\rm eff} - \log g$ diagram (Mucciarelli et al. 2022) and has not experienced the mixing episode that occurs at the red giant branch (RGB) bump. Therefore, the chemical composition is expected to be that of the natal cloud. Thus, the metallicity is so low that several SNe, or even just one, are enough to yield all the metals measured in the stellar atmospheres (Umeda & Nomoto 2003; Bonifacio et al. 2003; Limongi et al. 2003). The observed carbon abundances in CEMP-no stars are believed to come from faint SNe with energies of 10^{51} erg where fallback and mixing mechanisms played a role (Umeda & Nomoto 2003). Bonifacio et al. (2015) proposed an alternative explanation invoking a double source: lighter elements, typically CNO, synthesised by faint SNe as well as heavier elements, some α's included, synthesised by classical core-collapse SNe. For HE 0107−5240 we provide more stringent upper limits for the neutron-capture elements and a first measure of the ^{12}C/^{13}C. Hansen et al. (2015) find evidence of a 'floor' in the absolute Ba abundance of CEMP-no stars at the abundance level of A(Ba) ≈ -2. The existence of such a plateau was considered a specific feature of the CEMP-no stars and related to their progenitors. Both 'spinstar' models (i.e. metal-poor stars rotating fast; Meynet et al. 2006; Choplin et al. 2018) and mixing and fallback models (Umeda & Nomoto 2003; Nomoto et al. 2013) predict the production of an important amount of neutron-capture elements, which apparently are not seen in HE 0107−5240. This is generally interpreted as a minimum amount of Ba produced by the spinstars (Cescutti et al. 2016). The present upper limit of A(Ba) < -3.17 derived here is more than an order of magnitude below the level of the suggested floor value and provides evidence of a much reduced n-capture element production by the early generation of stars.

9.3. The isotopic ratio $^{12}C/^{13}C$

In HE 0107−5240 we have been able to measure the ^{12}C/^{13}C ratio. ^{12}C is a primary product of stellar nucleosynthesis and is formed in the triple-α process during hydrostatic helium burning. The stable ^{13}C isotope is produced in the hydrogen-burning shell when the CN cycle converts ^{12}C into ^{13}C. These processes, which occur mainly in intermediate-mass stars that develop as AGB stars (Wannier 1980), lead to a CN−cycle equilibrium ratio of about ^{12}C/^{13}C $=\sim 3.4$. Large quantities of ^{13}C could also be produced by low-metallicity, massive, fast-rotating stars, which should mostly affect the early chemical evolution (Meynet et al. 2006; Limongi & Chieffi 2018; Maeder et al. 2015). Meynet et al. (2006) showed that the isotope composition in the stellar wind is characterised by very low values of ^{12}C/^{13}C $\sim 3-5$. Due to the contribution of relatively long-lived stars, chemical evolution models of the Galaxy predict a decrease in the isotopic ratio ^{12}C/^{13}C with time, and an increase with galactocentric distances (Romano & Matteucci 2003). In fact, the photospheric solar ratio ^{12}C/^{13}C$= 95 \pm 5$ (Asplund et al. 2006) is higher than the value found in local molecular clouds (^{12}C/^{13}C$\sim$ 60−70; Goto et al. 2003; Milam et al. 2005) and is significantly higher than that measured in the Galactic centre by Wilson & Matteucci (1992), ^{12}C/^{13}C$= 25 \pm 5$.

At high redshifts, carbon abundance had been measured in metal-poor damped Lyα (DLA) systems. Welsh et al. (2020) reported a bound on the carbon isotope ratio ^{12}C/^{13}C > 2.3 (2σ) in a DLA system at $z = 2.34$. They also find tentative evidence that the most metal-poor DLA population exhibits somewhat higher [C/O] values at redshift $z \lesssim 3$ with a potential upward trend in the ratio as redshift decreases. They argued that the elevated [C/O] ratios at $z \lesssim 3$ might be a signature of enrichment from the first metal-enriched low- and intermediate-mass stars. At somewhat lower redshifts there are few determinations of the carbon isotopic ratio. Muller et al. (2006) obtained a ^{12}C/^{13}C ratio of 27 ± 2 in the Galaxy at $z_{\rm abs} = 0.89$ using the C I transitions. Levshakov et al. (2006) obtained ^{12}C/^{13}C> 80 in the $z_{\rm abs} = 1.15$ DLA towards HE 0515−4414, implying a very low ^{13}C abundance. Carswell et al. (2011) in the $z_{\rm abs} = 1.7764$ DLA system towards J1331+170, which is also the system we are studying here by means of new ESPRESSO observations, derived ^{12}C/^{13}C > 5 (2σ).

Hansen et al. (2015) and Norris et al. (2013) measured the ^{12}C/^{13}C in a sample of CEMP stars. Most of them have low ^{12}C/^{13}C as a result of high ^{13}C, but they also show [C/N] < 0, which is evidence of internal mixing according to Spite et al. (2006). HE 0107−5240 shows [C/N] > 0 and therefore is unmixed. Consequently, the new measure of ^{12}C/^{13}C $= 87 \pm 6$ implies that the low ^{13}C is pristine. This suggests that the parent generation of stars that polluted the material from which this star was born did not produce any significant amount of ^{13}C. Spinstar models (Meynet et al. 2006), which predict production of an important amount of ^{13}C, are therefore not favoured.

9.4. Lithium during the HE 0107−5240 evolution

The upper limit of Li in HE 0107−5240 is also improved to A(Li) < 0.5 with a confidence level higher than 3σ. HE 0107−5240 is in the LRGB, which includes stars with $2 \leq \log g \leq 3$ located after the first dredge-up (FDU) and before the RGB-bump luminosity. Assuming these stars start with the same initial Li abundance, the present Li abundance depends on how much Li has been destroyed in the extension of the convection zone during the FDU. Mucciarelli et al. (2022) find that the majority of LRGB stars show a very thin plateau in the Li abundance with A(Li) $= 1.09 \pm 0.07$ and that this results from the stellar dilution in the giant evolution. They also find that a small fraction of stars, about 20%, show no detectable Li, namely A(Li) ≤ 0.7. For HE 0107−5240 Mucciarelli et al. (2022) derived A(Li) ≤ 0.7, which we improve slightly to A(Li) ≤ 0.5. This bound places HE 0107−5240 in the minority of stars without any Li signature. Another LRGB star we are investigating for RV changes, HE 0557−4840, also shows an absence of Li, with A(Li) < 0.60 (Mucciarelli et al. 2022). It is not clear for these stars if they were originally Li-poor objects or if they suffered from extra destruction of Li either during the main sequence or the post-main-sequence evolution. However, this seems uncorrelated with metallicity since Li has also been measured at A(Li) $= 0.87 \pm 0.05$ in SMSS J0313−6708, which, with [Fe/H] < -7.0, is the lowest-metallicity star known; therefore, a similar abundance is also expected in the other, more metal-rich subgiants. Since theoretically there is no known mechanism that can destroy Li in the main sequence or in the RGB before the RGB bump, there are three main scenarios left to explain the metal-poor CEMP-no stars with no or low Li detection.

First, the gas from which the star was formed was Li-free. This may be the case if the star was formed from almost pure SN ejecta, with very little dilution by primordial gas.

Second, Li was destroyed in the pre-main-sequence phase (Fu et al. 2015). This phase is not easily modelled, and the question remains as to what the different was during the pre-main-sequence phase of these stars with respect to that of other stars that retained Li. In Fu et al. (2015) the model of the resulting Li

is a balance between pre-main-sequence destruction and partial accretion of gas with Li at the primordial value. In general, these stars are less massive for a given $T_{\rm eff}$, and such a balance could have been broken.

Third, the star is an evolved blue straggler. Ryan et al. (2001) suggested that unevolved metal-poor stars with no detectable Li were 'blue-stragglers-to-be', and in fact *Gaia* parallaxes have shown that three out of four stars studied by Ryan et al. (2001) are indeed 'canonical' blue stragglers (Bonifacio et al. 2018a). If this were true in the case of HE 0107-5240, we should postulate that the system was initially a hierarchical triple system with an inner pair that eventually coalesced to form a blue straggler and an outer companion that is the companion presently revealed by the orbital motion.

Bonifacio et al. (2018b) and Aguado et al. (2019) studied several dwarf stars with extremely low metallicity, and only three out of the eight dwarfs with [Fe/H] < −4.2 have detectable Li close to, albeit below, the Spite plateau. It is therefore very likely that the high fraction of Li-depleted stars is related to the significant Li destruction by the progenitor responsible for the high carbon abundances observed in the CEMP-no stars.

9.5. Consequences for the nature of CEMP-no stars

The lack of binaries among the CEMP-no stars holds important clues on the star formation of stars from primordial or nearly primordial chemistry. At the time of the discovery of HE 0107−5240, the possibility of low-mass star forming from almost metal-free gas was not conceived of (Palla 2003). In the conventional model of primordial star formation, H_2 cooling of metal-free gas leads to the formation of massive stars with a characteristic stellar mass of $\approx$100 $M_\odot$.

The discovery of the extremely metal-poor CEMP-no stars led to a revision of the processes for the formation of low-mass stars. Bromm & Loeb (2003) suggested that atomic lines of neutral oxygen and singly ionised carbon could effectively cool a very metal-poor contracting cloud, provided the abundance of these elements is at the level observed in the CEMP stars. However, the successive discovery of two extremely metal-poor stars that are not carbon-enhanced (Caffau et al. 2011a; Starkenburg et al. 2018) suggests that metal-line cooling cannot be the only mechanism capable of leading the formation of a sub-solar mass at very low metallicity. Smaller masses of the order of 1 $M_\odot$ may only be obtained by dust cooling. However, recent refinements in the modelling of the collapse process of primordial star formation have shown that the original clouds are prone to fragmentation (Greif 2015). This leads more likely to the formation of a massive central star or a binary system surrounded by some low-mass stars. The simulation of Becerra et al. (2015) of a cooling primordial cloud found that the fragmentation of the disc around the initial protostar could generate a second protostellar system with five to ten members with masses of the order of 1 $M_\odot$. They also showed that, at the end of the simulation, the collapse could evolve into a wide binary system with a distance of hundreds of AU. The confirmation of the binarity of HE 0107−5240, which is one of the most metal-poor stars known, shows that the process of star formation in very metal-poor gas could lead to the formation of binaries. However, the majority of single stars show that these initial clusters probably dispersed or did not end up preferentially in binary systems.

10. Conclusions

We summarise here the main conclusions:

- Over 3 yr we observed eight of the most metal-poor CEMP-no stars with ESPRESSO to probe binarity by means of very accurate RVs.
- Out of these, only HE 0107−5240 showed clear evidence for an orbital motion. HE 0107−5240 shows a monotonic decreasing trend in RV at a rate of approximately 0.5 m s^{-1} d^{-1}. The maximum $v_{\rm rad}$ was reached between March 13, 2012, and December 8, 2014, and the period is constrained at $P_{\rm orb} = 13009^{+1496}_{-1370}$ d. The $v_{\rm rad}$ for the other six CEMP-no stars are consistent with single stars, while there is solid indication of binarity behaviour in SMSS 1605−1443 with an approximate $v_{\rm rad}$ variation of ∼1.6 m s^{-1} d^{-1}.
- Speckle observations of HE 0107−5240 do not reveal companions at distances greater than 1000 AU.
- Revised chemistry of HE 0107−5240 provided more stringent upper limits to [Sr/Fe] < −0.76 and [Ba/Fe] < +0.20, confirming the star as a CEMP-no. The isotopic ratio ^{12}C/^{13}C is measured for the first time in an unmixed giant and found to be close to the solar value. The low ^{13}C is in contrast to what is expected from a spinstar progenitor. The measurement of lithium is also improved to a value of A(Li) < 0.5, well below the Li plateau at 1.1 found in the LRGB stars by Mucciarelli et al. (2022), suggesting the star was originally depleted by lithium.
- The fact that there are some binaries among the CEMP-no group (HE 0107−5240, SDSS J0929+0238, and likely SMSS 1605−1443) indicates that low metallicity does not inhibit the formation of binaries.

We conclude by saying that this successful programme with ESPRESSO must continue in order to understand the ultimate nature of the primitive CEMP-no stars and its relation with the earliest stages of the chemical evolution.

Acknowledgements. The authors wish to thank the Gemini Director for the allocation of engineering time to perform this observation. DA would like to thank Dr. Megan Bedell for her enjoyable discussion of the ESPRESSO data at the Flatiron Institute. DA also acknowledges support from the ERC Starting Grant NEFERTITI H2020/808240. JIGH, CAP, ASM and RR acknowledge financial support from the Spanish Ministry of Science and Innovation (MICINN) project PID2020-117493GB-I00. JIGH also acknowledges financial support from the Spanish MICINN under 2013 Ramón y Cajal program RYC-2013-14875. ASM acknowledges financial support from the Spanish Ministry of Science and Innovation (MICINN) under 2018 Juan de la Cierva program IJC2018-035229-I. Zorro was funded by the NASA Exoplanet Exploration Program and built at the NASA Ames Research Center by Steve B. Howell, Nic Scott, Elliott P. Horch, and Emmett Quigley. Gemini Observatory is a program of NSF's NOIRLab, which is managed by the Association of Universities for Research in Astronomy (AURA) under a cooperative agreement with the National Science Foundation. on behalf of the Gemini partnership: the National Science Foundation (United States), National Research Council (Canada), Agencia Nacional de Investigación y Desarrollo (Chile), Ministerio de Ciencia, Tecnología e Innovación (Argentina), Ministério da Ciência, Tecnologia, Inovações e Comunicações (Brazil), and Korea Astronomy and Space Science Institute (Republic of Korea). This work was supported by FCT – Fundação para a Ciência e a Tecnologia through national funds and by FEDER through COMPETE2020–Programa Operacional Competitividade e Internacionalizaçào by these grants: UID/FIS/04434/2019; UIDB/04434/2020; UIDP/04434/2020; PTDC/FIS-AST/32113/2017 & POCI-01-0145-FEDER-032113. CJM also acknowledges FCT and POCH/FSE (EC) support through Investigador FCT Contract 2021.01214.CEECIND/CP1658/CT0001. This work has made use of data from the European Space Agency (ESA) mission *Gaia* (https://www.cosmos.esa.int/gaia), processed by the *Gaia* Data Processing and Analysis Consortium (DPAC, https://www.cosmos.esa.int/web/gaia/dpac/consortium). Funding for the DPAC has been provided by national institutions, in particular the institutions participating in the *Gaia* Multilateral Agreement. This work was financed by FEDER-Fundo Europeu de Desenvolvimento Regional funds through the COMPETE 2020-Operational Programme for Competitiveness and Internationalisation (POCI), and by Portuguese funds through FCT–Fundação para a Ciência e a Tecnologia under projects POCI-01-0145-FEDER-028987, PTDC/FIS-AST/28987/2017, PTDC/FIS-AST/0054/2021 and

EXPL/FIS-AST/1368/2021, as well as UIDB/04434/2020 & UIDP/04434/2020, CERN/FIS-PAR/0037/2019, PTDC/FIS-OUT/29048/2017. FPE and CLO would like to acknowledge the Swiss National Science Foundation (SNSF) for supporting research with ESPRESSO through the SNSF grants nr. 140649, 152721, 166227 and 184618. The ESPRESSO Instrument Project was partially funded through SNSF's FLARE Programme for large infrastructures. MTM acknowledges the support of the Australian Research Council through Future Fellowship grant FT180100194

References

Aguado, D. S., Allende Prieto, C., González Hernández, J. I., Rebolo, R., & Caffau, E. 2017, A&A, 604, A9
Aguado, D. S., González Hernández, J. I., Allende Prieto, C., & Rebolo, R. 2018a, ApJ, 852, L20
Aguado, D. S., Allende Prieto, C., González Hernández, J. I., & Rebolo, R. 2018b, ApJ, 854, L34
Aguado, D. S., González Hernández, J. I., Allende Prieto, C., & Rebolo, R. 2019, ApJ, 874, L21
Allende Prieto, C., Fernández-Alvar, E., Aguado, D. S., et al. 2015, A&A, 579, A98
Arentsen, A., Starkenburg, E., Shetrone, M. D., et al. 2019, A&A, 621, A108
Asplund, M., Grevesse, N., & Jacques Sauval, A. 2006, Nucl. Phys. A, 777, 1
Barentsen, G., Hedges, C., Vinícius, Z., et al. 2021, https://doi.org/10.5281/zenodo.1181928
Becerra, F., Greif, T. H., Springel, V., & Hernquist, L. E. 2015, MNRAS, 446, 2380
Beers, T. C., & Christlieb, N. 2005, Highlights Astron., 13, 579
Bianchi, L., Herald, J., Efremova, B., et al. 2011, Ap&SS, 335, 161
Bonifacio, P., Molaro, P., Beers, T. C., & Vladilo, G. 1998, A&A, 332, 672
Bonifacio, P., Limongi, M., & Chieffi, A. 2003, Nature, 422, 834
Bonifacio, P., Caffau, E., Spite, M., et al. 2015, A&A, 579, A28
Bonifacio, P., Caffau, E., Spite, M., et al. 2018a, Res. Notes Am. Astron. Soc., 2, 19
Bonifacio, P., Caffau, E., Spite, M., et al. 2018b, A&A, 612, A65
Bonifacio, P., Molaro, P., Adibekyan, V., et al. 2020, A&A, 633, A129
Bromm, V., & Loeb, A. 2003, Nature, 425, 812
Caffau, E., Bonifacio, P., François, P., et al. 2011a, Nature, 477, 67
Caffau, E., Ludwig, H. G., Steffen, M., Freytag, B., & Bonifacio, P. 2011b, Sol. Phys., 268, 255
Caffau, E., Bonifacio, P., Spite, M., et al. 2016, A&A, 595, L6
Carswell, R. F., Jorgenson, R. A., Wolfe, A. M., & Murphy, M. T. 2011, MNRAS, 411, 2319
Cayrel, R. 2005, Nature, 434, 838
Ceillier, T., Tayar, J., Mathur, S., et al. 2017, A&A, 605, A111
Cescutti, G., Valentini, M., François, P., et al. 2016, A&A, 595, A91
Chiaki, G., Tominaga, N., & Nozawa, T. 2017, MNRAS, 472, L115
Choplin, A., Hirschi, R., Meynet, G., et al. 2018, A&A, 618, A133
Christlieb, N., Green, P. J., Wisotzki, L., & Reimers, D. 2001, A&A, 375, 366
Christlieb, N., Bessell, M. S., Beers, T. C., et al. 2002a, Nature, 419, 904
Christlieb, N., Wisotzki, L., & Graßhoff, G. 2002b, A&A, 391, 397
Christlieb, N., Gustafsson, B., Korn, A. J., et al. 2004, APJ, 603, 708
Collet, R., Asplund, M., & Trampedach, R. 2006, ApJ, 644, L121
Creevey, O., Grundahl, F., Thévenin, F., et al. 2019, A&A, 625, A33
Foreman-Mackey, D., Agol, E., Ambikasaran, S., & Angus, R. 2017, AJ, 154, 220
Frebel, A., Aoki, W., Christlieb, N., et al. 2005, Nature, 434, 871
Frebel, A., Chiti, A., Ji, A. P., Jacobson, H. R., & Placco, V. M. 2015, ApJ, 810, L27
Frebel, A., Ji, A. P., Ezzeddine, R., et al. 2019, ApJ, 871, 146
Fu, X., Bressan, A., Molaro, P., & Marigo, P. 2015, MNRAS, 452, 3256
Fulton, B. J., Petigura, E. A., Blunt, S., & Sinukoff, E. 2018, PASP, 130, 044504
Gaia Collaboration (Brown, A. G. A., et al.) 2021, A&A, 649, A1
González Hernández, J. I., Aguado, D. S., Allende Prieto, C., Burgasser, A. J., & Rebolo, R. 2020, ApJ, 889, L13
Goto, M., Usuda, T., Takato, N., et al. 2003, ApJ, 598, 1038
Greif, T. H. 2015, Comput. Astrophys. Cosmol., 2, 3
Greif, T. H., Bromm, V., Clark, P. C., et al. 2012, MNRAS, 424, 399
Hansen, T., Hansen, C. J., Christlieb, N., et al. 2014, ApJ, 787, 162
Hansen, T., Hansen, C. J., Christlieb, N., et al. 2015, ApJ, 807, 173
Hansen, C. J., Nordström, B., Hansen, T. T., et al. 2016a, A&A, 588, A37
Hansen, T. T., Andersen, J., Nordström, B., et al. 2016b, A&A, 586, A160
Howell, S. B., & Furlan, E. 2022, Front. Astron. Space Sci., 9, 871163
Howell, S. B., Everett, M. E., Sherry, W., Horch, E., & Ciardi, D. R. 2011, AJ, 142, 19
Jofré, P., Heiter, U., Soubiran, C., et al. 2014, A&A, 564, A133
Johnson, J. L., & Li, H. 2012, ApJ, 751, 81
Keller, S. C., Bessell, M. S., Frebel, A., et al. 2014, Nature, 506, 463
Kurucz, R. L. 2005, Mem. Soc. Astron. It. Suppl., 8, 14
Levshakov, S. A., Centurión, M., Molaro, P., & Kostina, M. V. 2006, A&A, 447, L21
Limongi, M., & Chieffi, A. 2018, ApJS, 237, 13
Limongi, M., Chieffi, A., & Bonifacio, P. 2003, ApJ, 594, L123
Lodders, K. 2019, Nuclei in the Cosmos XV, 219, 165
Maeder, A., Meynet, G., & Chiappini, C. 2015, A&A, 576, A56
Marconi, M., Musella, I., Fiorentino, G., et al. 2010, ApJ, 713, 615
Meynet, G., Ekström, S., & Maeder, A. 2006, A&A, 447, 623
Milam, S. N., Savage, C., Brewster, M. A., Ziurys, L. M., & Wyckoff, S. 2005, ApJ, 634, 1126
Mucciarelli, A., Monaco, L., Bonifacio, P., et al. 2022, A&A, 661, A153
Muller, S., Guélin, M., Dumke, M., Lucas, R., & Combes, F. 2006, A&A, 458, 417
Nomoto, K., Kobayashi, C., & Tominaga, N. 2013, ARA&A, 51, 457
Nordlander, T., Bessell, M. S., Da Costa, G. S., et al. 2019, MNRAS, 488, L109
Norris, J. E., Ryan, S. G., & Beers, T. C. 1997, ApJ, 489, L169
Norris, J. E., Christlieb, N., Korn, A. J., et al. 2007, ApJ, 670, 774
Norris, J. E., Yong, D., Bessell, M. S., et al. 2013, ApJ, 762, 28
Palla, F. 2003, Mem. Soc. Astron. It. Suppl., 3, 52
Pepe, F., Cristiani, S., Rebolo, R., et al. 2013, The Messenger, 153, 6
Pepe, F., Cristiani, S., Rebolo, R., et al. 2021, A&A, 645, A96
Preston, G. W., & Sneden, C. 2001, AJ, 122, 1545
Ricker, G. R., Winn, J. N., Vanderspek, R., et al. 2015, J. Astron. Telesc. Instrum. Syst., 1, 014003
Romano, D., & Matteucci, F. 2003, MNRAS, 342, 185
Ryan, S. G., Beers, T. C., Kajino, T., & Rosolankova, K. 2001, ApJ, 547, 231
Sbordone, L. 2005, Mem. Soc. Astron. It. Suppl., 8, 61
Scargle, J. D. 1982, ApJ, 263, 835
Schneider, R., Ferrara, A., Salvaterra, R., Omukai, K., & Bromm, V. 2003, Nature, 422, 869
Schneider, R., Omukai, K., Bianchi, S., & Valiante, R. 2012, MNRAS, 419, 1566
Scott, N. J., Howell, S. B., Gnilka, C. L., et al. 2021, Front. Astron. Space Sci., 8, 138
Speagle, J. S. 2020, MNRAS, 493, 3132
Spite, M., Cayrel, R., Hill, V., et al. 2006, A&A, 455, 291
Spite, M., Caffau, E., Bonifacio, P., et al. 2013, A&A, 552, A107
Starkenburg, E., Aguado, D. S., Bonifacio, P., et al. 2018, MNRAS, 481, 3838
Suda, T., Aikawa, M., Machida, M. N., Fujimoto, M. Y., Iben, Icko, & J., 2004, ApJ, 611, 476
Tauris, T. M., & van den Heuvel, E. P. J. 2006, Compact Stellar X-ray Sources, 39, 623
Tody, D. 1993, ASP Conf. Ser., 52, 173
Tonry, J., & Davis, M. 1979, AJ, 84, 1511
Tsantaki, M., Pancino, E., Marrese, P., et al. 2022, A&A, 659, A95
Umeda, H., & Nomoto, K. 2003, Nature, 422, 871
Venn, K. A., Puzia, T. H., Divell, M., et al. 2014, ApJ, 791, 98
Wannier, P. G. 1980, ARA&A, 18, 399
Welsh, L., Cooke, R., Fumagalli, M., & Pettini, M. 2020, MNRAS, 494, 1411
Wilson, T. L., & Matteucci, F. 1992, A&ARv, 4, 1
Yoon, J., Beers, T. C., Placco, V. M., et al. 2016, ApJ, 833, 20
Yoon, J., Beers, T. C., Tian, D., & Whitten, D. D. 2019, ApJ, 878, 97
Zechmeister, M., & Kürster, M. 2009, A&A, 496, 577

[1] Dipartimento di Fisica e Astronomia, Universit á degli Studi di Firenze, Via G. Sansone 1, 50019 Sesto Fiorentino, Italy
e-mail: david.aguado@unifi.it
[2] INAF-Osservatorio Astrofisico di Arcetri, Largo E. Fermi 5, 50125 Firenze, Italy
[3] INAF-Osservatorio Astronomico di Trieste, Via G.B. Tiepolo 11, 34143 Trieste, Italy
[4] Institute of Fundamental Physics of the Universe, Via Beirut 2, Miramare, 34151 Trieste, Italy
[5] GEPI, Observatoire de Paris, Université PSL, CNRS, 5 Place Jules Janssen, 92190 Meudon, France
[6] Instituto de Astrofísica de Canarias, Vía Láctea, 38205 La Laguna, Tenerife, Spain
[7] Universidad de La Laguna, Departamento de Astrofísica, 38206 La Laguna, Tenerife, Spain
[8] Centro de Astrobiología (CSIC-INTA), Carretera Ajalvir km 4, 28850 Torrejón de Ardoz, Madrid, Spain

[9] Consejo Superior de Investigaciones Científicas, 28006 Madrid, Spain
[10] INAF – Osservatorio Astrofisico di Torino, Via Osservatorio 20, 10025 Pino Torinese, Italy
[11] NASA Ames Research Center, Moffett Field, CA 94035, USA
[12] NASA Exoplanet Science Institute, Caltech/IPAC, Mail Code 100-22, 1200 E. California Blvd., Pasadena, CA 91125, USA
[13] Scuola Normale Superiore Piazza dei Cavalieri, Pisa 7 56126, Italy
[14] Instituto de Astrofísica e Ciências do Espaço, Faculdade de Ciências da Universidade de Lisboa, Campo Grande, 1749-016 Lisboa, Portugal
[15] Instituto de Astrofísica e Ciências do Espaço, CAUP, Universidade do Porto, Rua das Estrelas, 4150-762 Porto, Portugal
[16] Centro de Astrofísica da Universidade do Porto, Rua das Estrelas, 4150-762 Porto, Portugal
[17] INFN, Sezione di Trieste, Via Valerio 2, I-34127 Trieste, Italy
[18] Centre for Astrophysics and Supercomputing, Swinburne University of Technology, Hawthorn, Victoria 3122, Australia
[19] Observatoire Astronomique de l'Université de Genève, Chemin Pegasi 51, Sauverny 1290, Switzerland
[20] Département d'astronomie de l'Université de Genève, Chemin Pegasi 51, 1290 Versoix, Switzerland
[21] Instituto de Astrofísica e Ciências do Espaço, CAUP, Universidadedo Porto, Rua das Estrelas, 4150-762 Porto, Portugal
[22] Departamento de Física e Astronomia, Faculdade de Ciências, Universidade do Porto, Rua Campo Alegre, 4169-007 Porto, Portugal